nature communications

Article

https://doi.org/10.1038/s41467-025-62195-x

Na-alloy tailored 3D/0D metal halide heterostructures enabling efficient charge transfer for color-integrated white scintillators

Received: 15 November 2024

Accepted: 11 July 2025

Published online: 26 July 2025

Check for updates

Zhi Yang[1] ✉, Jiangtao Cui[1], Ying Sun[1], Jisong Yao[1], Shuang Yang[2] & Jizhong Song[1] ✉

Lead-free halide perovskites featuring broad emissions have attracted increasing interest as X-ray imaging scintillators. Currently, the radioluminescence spectrum is primarily tuned by dopants and crystal fields, thus exploring a heterostructure manner to extensively modulate emission intensity and linewidth presents an exciting opportunity. Herein, we synthesize 3D/0D $Cs_2NaLuCl_6$/Cs_3LuCl_6(Sb) heterostructures via a Na-alloying strategy to tailor the spectral feature of scintillators. We find that type I heterostructure can promote the emission of 0D Cs_3LuCl_6(Sb) through charge transfer mechanism, as corroborated by the combination of energy band alignment, ultrafast transient dynamics, microscopic photoluminescence and electrical conductivity. As a result, 3D/0D scintillator exhibits a 1.8-times higher radioluminescence intensity than 0D scintillator. Meanwhile, featuring a spectrum-flat white emission, 3D/0D scintillator provides a balanced RGB output enabling to extend the dynamic range in color-integrated X-ray imaging. These findings provide insights into constructing metal halide heterostructures with efficient charge transfer, and advance the design and application of lead-free perovskites and their derivatives.

Density-discriminating X-ray imaging is pivotal in medical diagnostics, safety inspections, and industrial flaw detection, as it effectively differentiates between high-density and low-density components within an object based on X-ray absorption. For instance, this technique can distinguish between bones and muscles in biological organisms, metal parts and plastic casings in consumer products, and metallic circuits and resin substrates in electronic devices[1,2]. Recently, vertical matrix detector and stacked chromatic scintillator techniques[3–8] have been developed to address the issue of imperfect superimposition of dual-energy images in the dual-energy X-ray source technique. However, these techniques are significantly contingent upon the structural configurations of direct or indirect (scintillator) detectors. Hence, developing a color-integrated X-ray imaging technique utilizing the multi-color characteristic of a broad-spectrum scintillator to distinguish the object density will garner considerable interest, because it can lower hardware demands and expand the X-ray imaging capability of scintillators.

At present, lead-free perovskites and their derivatives are considered as efficient single-component white-emitting scintillators due to superior X-ray stopping power, tunable emission wavelength, and low-temperature synthesis[9–21]. Both lead-free $A_2B'(I)B''(III)X_6$ double perovskites with 3D crystal structure and $A_3B(III)X_6$ metal halide with

[1]Key Laboratory of Materials Physics of Ministry of Education, Laboratory of Zhongyuan Light, School of Physics, Zhengzhou University, Zhengzhou, China. [2]Key Laboratory for Ultrafine Materials of Ministry of Education, Shanghai Engineering Research Center of Hierarchical Nanomaterials, School of Materials Science and Engineering, East China University of Science and Technology, Shanghai, China. ✉e-mail: yanzh029@163.com; songjizhong@zzu.edu.cn

0D crystal structure have low electronic dimensions, therefore localized excitons can produce a strong electron-phonon coupling, forming self-trapped exciton (STE) emission with the features of broad emission, large Stokes shifts and high photoluminescence (PL) efficiency[22–24]. Optimizing dopants and engineering crystal fields are regular strategies to modulate the STE emission to achieve broad and bright emission. For example, 0D Cs_3LuCl_6 is sorted by a high-throughput screening to be a thermally robust inorganic phosphor due to a high Debye temperature (Θ_D) of 149 K, and tunable emission color and linewidth by doping Sb^{3+} or Ln^{3+} have been reported[25–27]. However, as a scintillator, the brightness of doped Cs_3LuCl_6 is still unsatisfactory although it has a high X-ray attenuation coefficient (Supplementary Note 1, Supplementary Fig. 1). For example, the Ce^{3+}-doped Cs_3LuCl_6 suffers from a low radioluminescence (RL) intensity[28,29], indicating that dopant-induced energy transfer is insufficient to guarantee a bright scintillator.

Unlike energy transfer via dopants, charge transfer provides another efficient route to enhance the emission intensity of acceptors

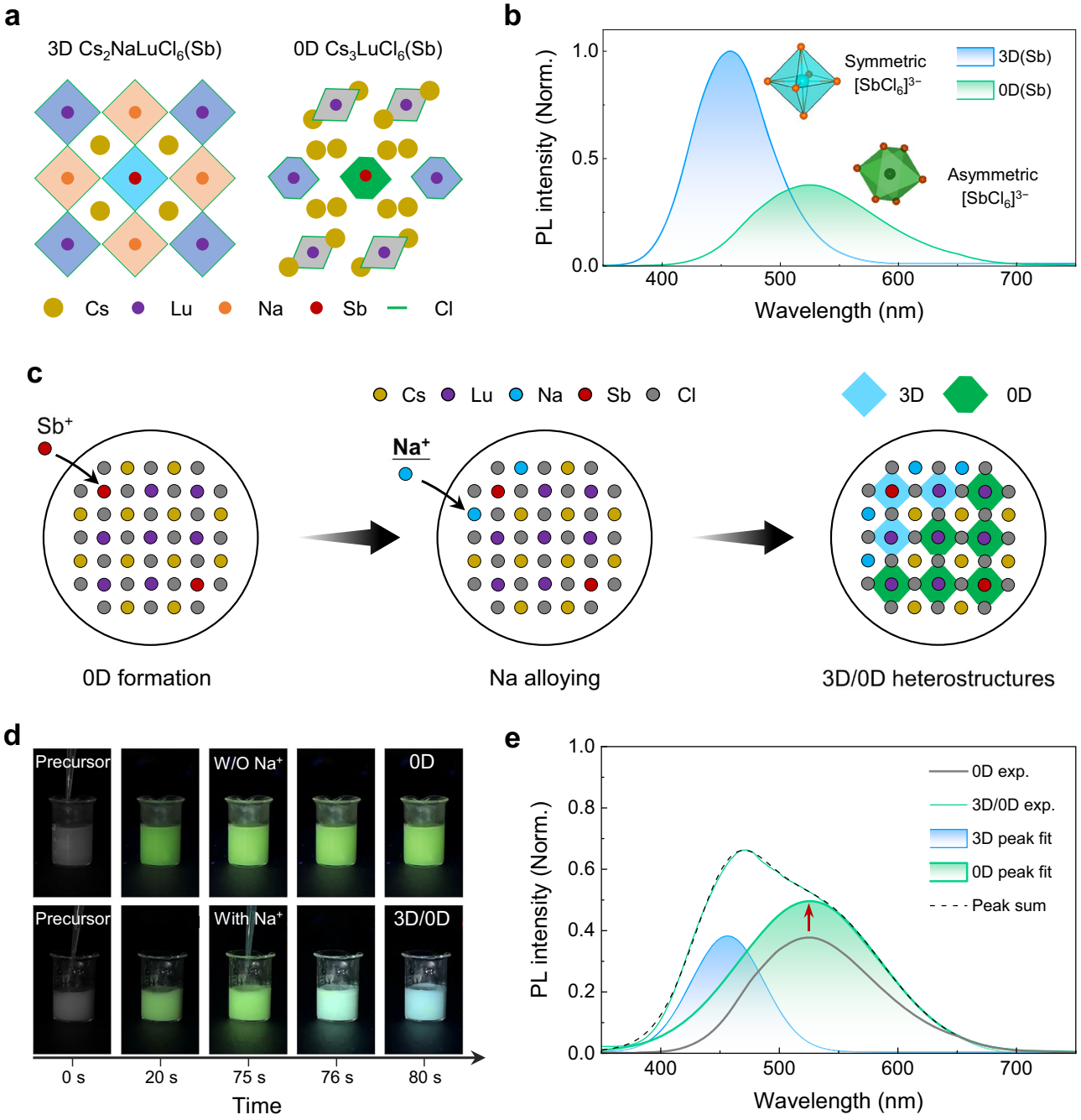

Fig. 1 | Design of 3D/0D heterostructures. a Crystal structures of 3D $Cs_2NaLuCl_6$(Sb) and 0D Cs_3LuCl_6(Sb). **b** PL spectra of 3D $Cs_2NaLuCl_6$(Sb) and 0D Cs_3LuCl_6(Sb) excited under 335 nm. The PL intensity of 3D perovskite is normalized to 1, and the relative intensity of 0D metal halide is shown. **c** A schematic diagram describing the formation of 3D/0D heterostructure through a Na-alloying strategy. **d** Photographs of 0D and 3D/0D heterostructure samples synthesized at the different reaction stages. $SbCl_3$ and NaCl solutions were added at 0 s and 75 s, respectively. The solutions were excited by a UV lamp. **e** PL spectra of 0D(Sb) and $3D_{0.3}/0D_{0.7}$(Sb) heterostructure excited under 335 nm. The PL intensity of 3D/0D heterostructure is determined based on the normalized 0D phase in (**b**). The PL spectra is fitted with the blue emission of 3D phase and the green emission of 0D phase.

https://doi.org/10.1038/s41467-025-62195-x

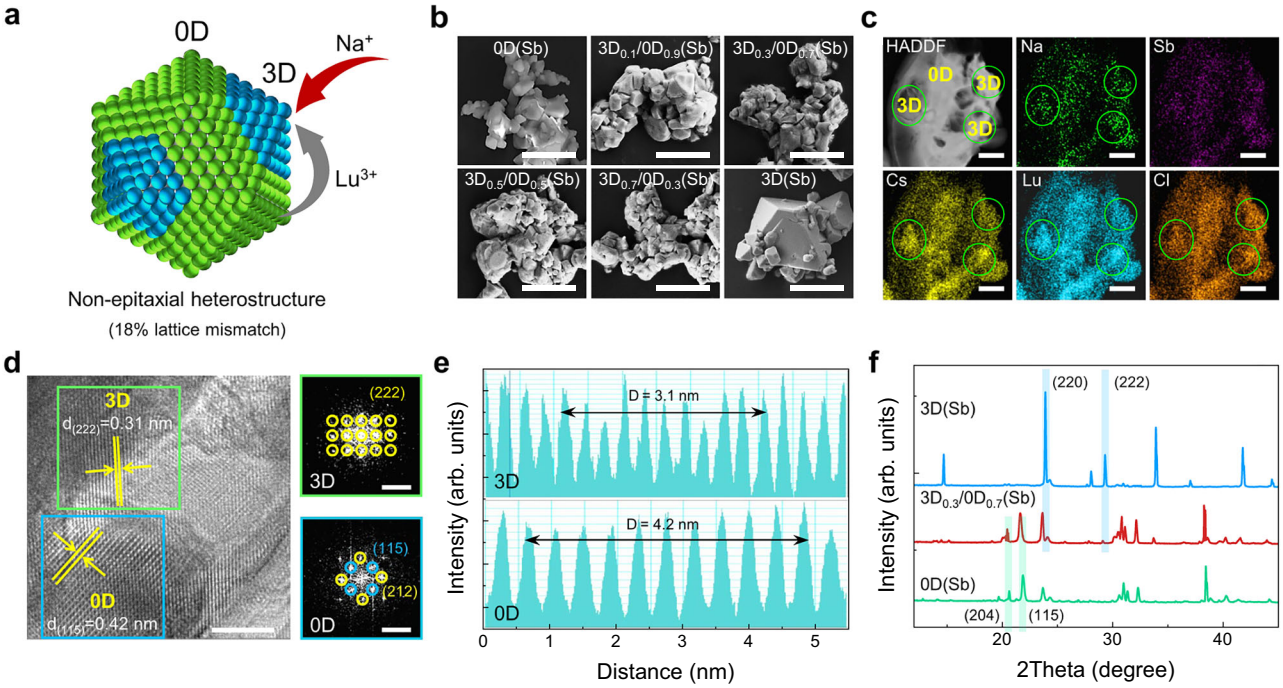

Fig. 2 | Microstructure characterization of 3D/0D heterostructures. a A schematic diagram of heterostructures synthesized by partially structural transform from 0D phase to 3D phase. **b** SEM images of 0D, 3D/0D and 3D particles, scale bars: 5 μm. **c** HAADF and elemental mapping, scale bars: 500 nm, **d** HRTEM image, scale bar: 5 nm; corresponding SAED patterns, scale bars: 5 nm^{-1}, and **e** intensity profiles of $3D_{0.3}/0D_{0.7}$(Sb) heterostructure. SAED patterns and intensity profiles are measured from the boxes shown in (**d**). 3D $Cs_2NaLuCl_6$ and 0D Cs_3LuCl_6 are identified based on the distribution of Na element in the elemental mapping (**c**). **f** XRD patterns of 3D $Cs_2NaLuCl_6$(Sb), 0D Cs_3LuCl_6(Sb) and $3D_{0.3}/0D_{0.7}$(Sb) heterostructure.

via constructing heterostructures. For example, $CsPbBr_3/Cs_4PbBr_6$ and $CsPbBr_3/CsPb_2Br_5$ heterostructures have been demonstrated to improve the RL intensity of scintillators based on the charge transfer from 0D or 2D phase to 3D perovskite under the built-in electric potential[30–32]. Extensively, heterostructure design has been demonstrated to effectively regulate the spectral features of Pb-based perovskite[33–37]. Therefore, leveraging charge transfer in lead-free perovskites is expected to promote the emission of acceptors, thereby improving the RL intensity of scintillators. However, the construction of type I heterostructures in lead-free perovskites has rarely been achieved, primarily due to the absence of a viable structural transformation route and matched energy band alignment between two phases. Thus, harnessing charge transfer to tailor the spectral intensity and linewidth of scintillators remains challenging.

In this work, we design a type I heterostructure scintillator, Sb^{3+} doped 3D/0D $Cs_2NaLuCl_6/Cs_3LuCl_6$, to simultaneously enhance the emission intensity and tailor the emission linewidth of 0D Cs_3LuCl_6(Sb). 3D/0D heterostructures are synthesized through a Na-alloying strategy, and the structural transformation from 0D Cs_3LuCl_6 to 3D $Cs_2NaLuCl_6$ is responsible for 3D/0D heterostructure formation, evidenced by the theoretical decomposition enthalpy and experimental color change and morphology analysis. 3D/0D heterostructures are engineered to leverage charge transfer mechanisms, which are revealed by combining the energy band alignment from electronic band structure calculation, the photogenerated carrier dynamics from transient absorption (TA) spectra and time-resolved PL (TRPL) spectra, the localized emission from PL mapping, and the electrical conductivity from current-voltage (*I-V*) measurement. Benefiting from the charge transfer in type I heterostructure, 3D/0D scintillator exhibits an increased RL intensity (2.4 times of $Bi_4Ge_3O_{12}$ (BGO)) compared to 0D scintillator (1.3 times of BGO). Importantly, 3D/0D heterostructure scintillator achieves a spectrum-flat broad white emission with a chromatic coordinate of (0.31, 0.32), resulting in the balanced RGB output signals (R, G, B = 0.83, 1, 0.91). With the assistance of a color-integrated X-ray imaging technique, the 3D/0D white scintillator shows the capability to distinguish object density.

Results and discussion

Synthesis and characterization of 3D/0D heterostructures

As presented in Fig. 1a and Supplementary Fig. 2, $Cs_2NaLuCl_6$(Sb) has a typical 3D double perovskite crystal structure, where $[LuCl_6]^{3-}$ octahedron and $[NaCl_6]^{5-}$ octahedron are separated by Cs^+ cations[38]. In contrast, Cs_3LuCl_6(Sb) has a 0D metal-halide crystal structure, where two kinds of $[LuCl_6]^{3-}$ octahedra are separated by Cs^+ cations[25]. Sb^{3+} ions are used as activators to enable the bright emission[39]. Typically, 3D $Cs_2NaLuCl_6$(Sb) has a blue emission centered at 455 nm while 0D Cs_3LuCl_6(Sb) has a green emission centered at 525 nm (Fig. 1b), because the symmetry of $[SbCl_6]^{3-}$ octahedra varies in different crystal fields, altering the dipole moments and thereby enabling the modulation of the Stokes-shift energy and emission wavelength[15,39,40]. More discussions on structure and PL spectra are given in Supplementary Note 2. In addition, the emission intensity of 0D Cs_3LuCl_6(Sb) is 0.4 times lower than that of 3D $Cs_2NaLuCl_6$(Sb) under the optimized Sb^{3+} doping (Fig. 1b, Supplementary Fig. 3). It is further evidenced by a lower PL quantum yield (PLQY) of 56% for 0D phase compared with that of 83% for 3D phase (Supplementary Fig. 4), in according with the report of $Cs_2NaInCl_6$(Sb)[40]. Thus, it is essential to improve the emission intensity of 0D Cs_3LuCl_6(Sb), which is expected to be realized through leveraging the charge transfer in type I heterostructures based on the excitation of 0D acceptor.

As shown in Fig. 1c, we propose a mechanism involving the structural transformation induced by Na-alloying for the formation of 3D/0D heterostructures. 0D(Sb) is firstly synthesized upon the introduction of Sb^+, and alloyed $Cs_{3-x}Na_xLuCl_6$ crystals[41] is subsequently formed following the addition of Na^+. As the Na^+ ratio increases, 3D $Cs_2NaLuCl_6$ crystals undergo enrichment followed by segregation

https://doi.org/10.1038/s41467-025-62195-x

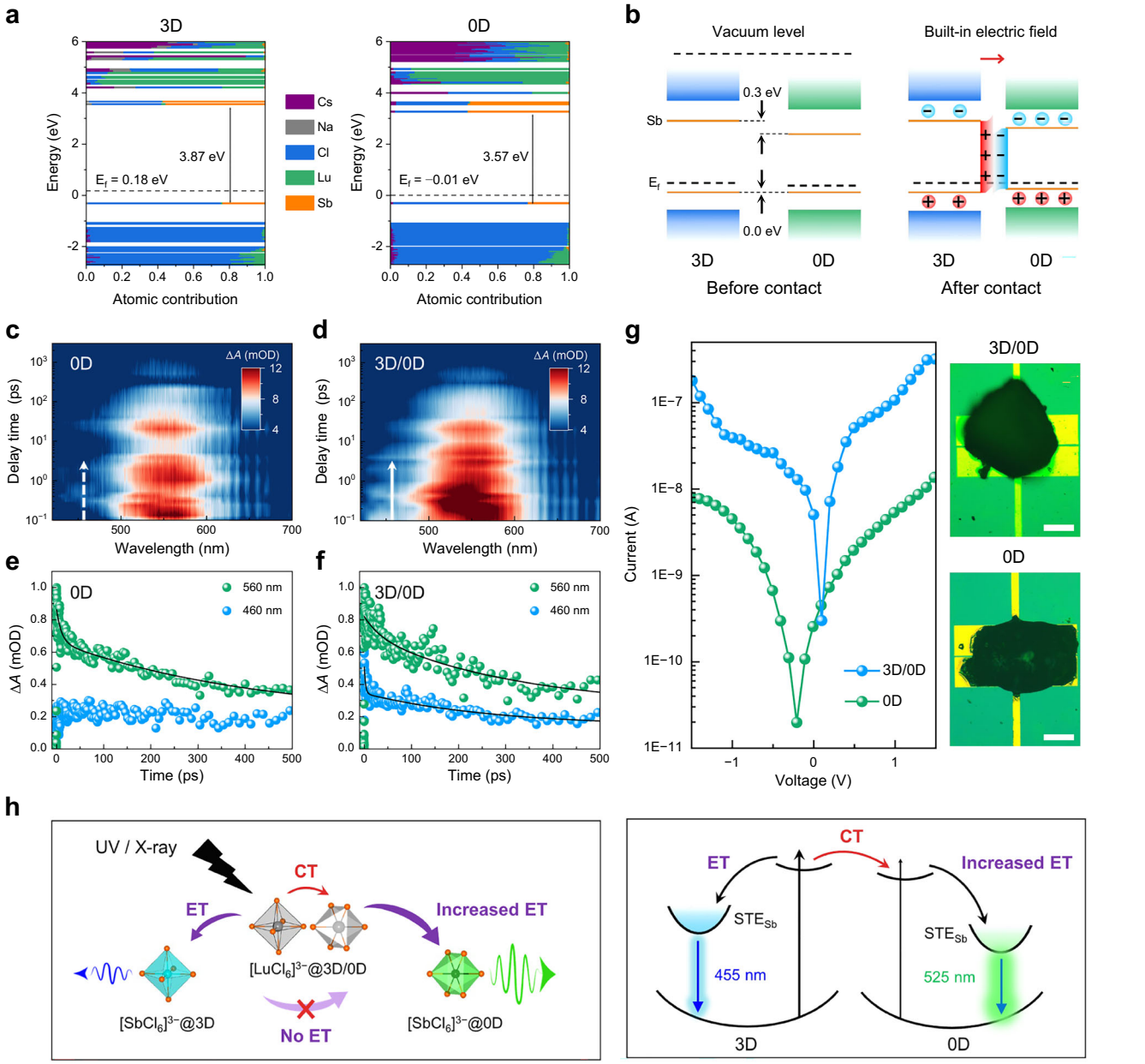

Fig. 3 | Luminescence mechanism of 3D/0D heterostructures. a Calculated electronic band structures of 3D $Cs_2NaLuCl_6$(Sb) and 0D Cs_3LuCl_6(Sb). **b** Energy band diagrams of 3D/0D heterostructure before and after contacts. Electrons are depleted in 3D side and diffused into 0D side, creating the built-in electric field from 3D phase to 0D phase, and holes are injected from 3D side into 0D side with the assistance of the built-in electric field. Time-wavelength-dependent TA color maps of (**c**) 0D phase and (**d**) 3D/0D heterostructure. TA spectra at a different wavelength as a function of delay time for (**e**) 0D phase and (**f**) 3D/0D heterostructure. **g** Current-voltage curves of single particle including 0D phase and 3D/0D heterostructure across a pair of Au electrodes with a 6 μm gap width. Scale bars: 100 μm. **h** Schematic diagrams of the luminescent mechanism for 3D/0D heterostructure under UV and X-ray excitations. CT charge transfer, ET energy transfer.

from the parent alloy crystals, driving the formation of 3D/0D heterostructures at the two-phase boundaries. The structural transformation from 0D to 3D is confirmed by the theoretical decomposition energy of 3D phase relative to 0D phase. The potential decomposition path is as follows:

$$3Cs_2NaLuCl_6 \rightarrow 2Cs_3LuCl_6 + 3NaCl + LuCl_3 \quad (1)$$

The 3D phase can be synthesized via the inverse reaction. The decomposition enthalpy (ΔH_d), which is defined via the following equation,

$$\Delta H_d = (2/3\,E[Cs_3LuCl_6] + E[NaCl] + 1/3\,E[LuCl_3] - E[Cs_2NaLuCl_6]) \quad (2)$$

The calculated ΔH_d is 0.76 eV. Here, the positive value of ΔH_d means that the decomposition process is endothermic, and the inverse reaction is exothermic, thereby indicating the easy formability of 3D $Cs_2NaLuCl_6$ from 0D Cs_3LuCl_6 induced by the introduction of Na^+.

The structural transformation is further evidenced by the color evolution in the synthesis process (Supplementary Fig. 5). We observe a gradually increased green emission from 0D Cs_3LuCl_6(Sb) along the progress of reaction. In contrast, the sample turns into pronounced cyan color quickly when Na^+ is introduced (Fig. 1d, Supplementary Movie 1), indicating the transformation from 0D phase to 3D phase. Importantly, we find Na^+ alloying occurs within 5 s, which is much faster than Sb^+ doping (~70 s). After the structural transformation, we observe that the increased green emission of 0D phase (Fig. 1e) in the 3D/0D heterostructure compared to individual 0D phase, suggesting the charge transfer from 3D donor to 0D acceptor.

The material structure was characterized by scanning electron microscopy (SEM), high-angle annular dark-field (HAADF), elemental mapping, and high-resolution transmission electron microscopy

https://doi.org/10.1038/s41467-025-62195-x

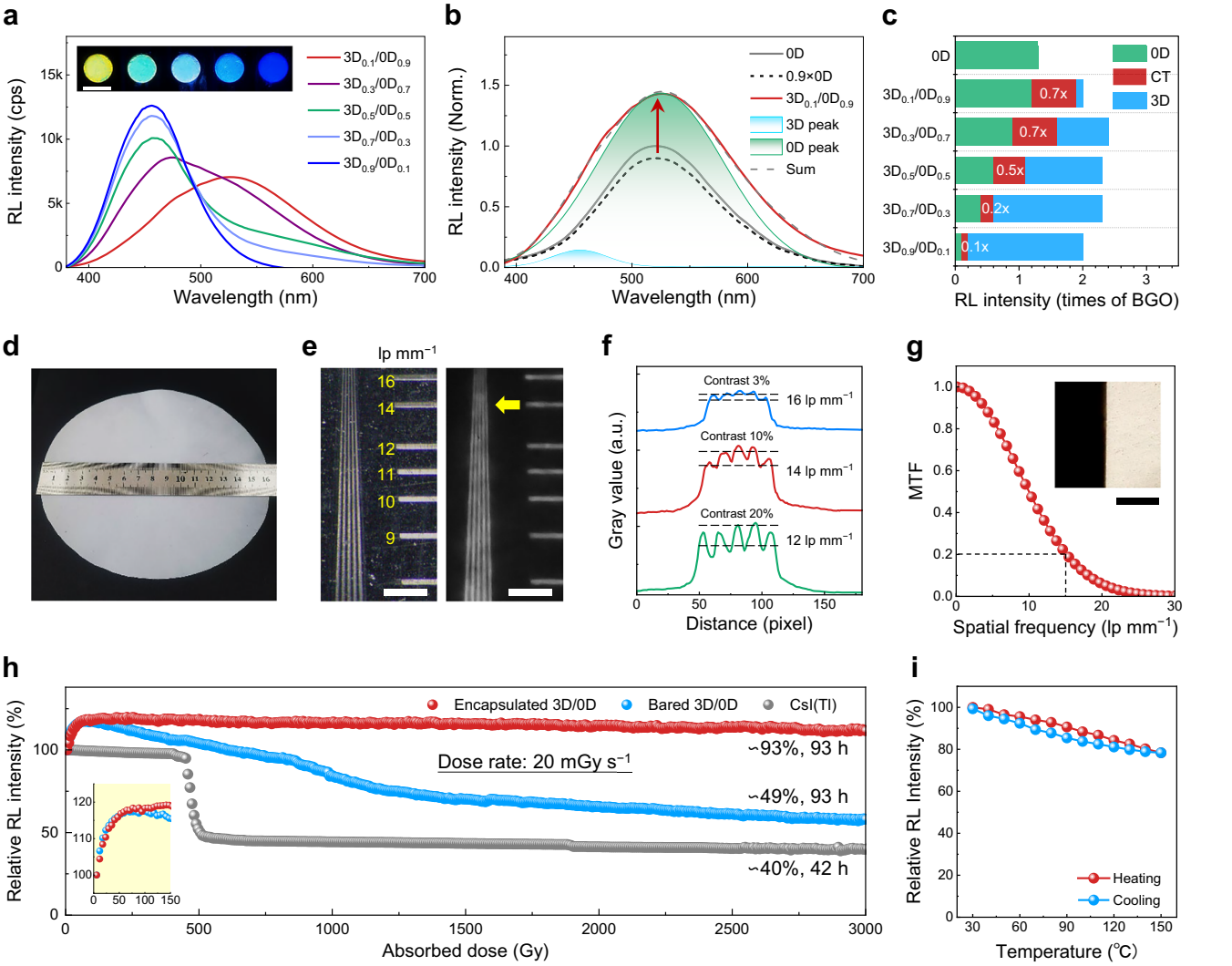

Fig. 4 | Scintillation performances of 3D/0D heterostructure scintillators. a RL spectra evolution of 3D/0D(3% Sb) heterostructure scintillators with different fractions. Inset is photographs of X-ray excited scintillators. Scale bar: 3 cm. **b** RL spectra of 0D and $3D_{0.1}/0D_{0.9}$ heterostructure scintillators. The RL spectra of heterostructure is fitted with the blue emission of 3D phase and the green emission of 0D phase. The RL intensity of 3D/0D scintillator is determined based on the normalized 0D scintillator. **c** Relative RL intensities of 0D and 3D/0D heterostructure scintillators compared with BGO. The RL emissions of heterostructure scintillators include self-0D emission, CT-induced 0D emission and 3D emission. The self-0D emission is calculated by multiplying the emission of pure 0D emission by their weight fraction because there is a linear relationship between RL intensity and weight within a certain range. Then, the CT-induced 0D emission (white numbers in (**c**)) is calculated by subtracting the self-0D emission from the fitted 0D emission. **d** Photograph of a large-area heterostructure scintillator screen. **e** Photographs of a standard line-pair card and the X-ray imaging of heterostructure scintillator. Scale bars: 1 mm. **f** Gray profiles of three line-pairs. **g** MTF curve, inset is the corresponding X-ray edge image. Scale bar: 1 mm. **h** X-ray irradiation stabilities of 3D/0D scintillators with and without encapsulation and commercial CsI(Tl) single crystal scintillator. Inset is the RL intensity evolution of 3D/0D scintillators during the initial dose accumulation up to 150 Gy. **i** RL intensity of 3D/0D scintillator as a function of temperature.

(HRTEM). Figure 2a describes that the 3D/0D heterostructure is formed through the partial transformation of 0D phase to 3D phase, induced by the introduction of Na^+. The formation of heterostructure is facilitated by the inherent soft lattice of metal halide perovskites, and only non-epitaxial heterostructure can be achieved due to a large lattice mismatch ratio of 18%. Figure 2b and Supplementary Fig. 6 shows 3D/0D heterostructures maintain the closed particle size with 0D phase although 3D phase has a larger particle size than 0D phase, because they are constructed by the structural transformation from 0D phase to 3D phase rather than the separate nucleation of two phases. As seen from the HAADF and elemental mapping in Fig. 2c, a single particle can confirm the formation of non-epitaxial 3D/0D heterostructures, which are further confirmed by the mixture of lattice planes in the HRTEM image (Fig. 2d). The distinct lattice plane fringes are assigned to the (222) crystal plane of 3D phase and the (115) crystal plane of 0D phase, corresponding to different SAED patterns and lattice plane distances (Fig. 2e). The actual ratio of 3D and 0D phases is in according with the nominal ratio, but the actual ratio of Sb^{3+} dopant is only 16% of the nominal value, indicating that Na alloying is easier completed than Sb^{3+} doping (Supplementary Fig. 7). The X-ray diffraction (XRD) patterns in Fig. 2f exhibit the cubic 3D phase[38,42] and monoclinic 0D phase[25], and 3D/0D heterostructures are the mixture of two phases. The crystalline structures of 3D/0D heterostructures gradually evolve from 0D phase to 3D phase with increasing Na^+ ratio (Supplementary Fig. 8).

Charge transfer mechanism

We performed density-functional theory (DFT) calculations and PL excitation (PLE) spectra to explore the electronic structures of 3D and 0D phases for constructing 3D/0D heterostructures. As shown in

Fig. 3a and Supplementary Fig. 9, $SbCl_6$ conduction band minimum (CBM), including Sb-s and Cl-p orbitals and $SbCl_6$ valence band maximum (VBM), including Sb-p and Cl-p orbitals, appear after Sb^{3+} are introduced, in according with that of $Cs_2NaInCl_6(Sb)$[43]. The $SbCl_6$ bandgap in 3D $Cs_2NaLuCl_6$ and 0D Cs_3LuCl_6 are 3.87 eV and 3.57 eV, respectively, which is further demonstrated by various PLE peaks for 3D (3.89 eV) and 0D (3.60 eV) (Supplementary Fig. 10). Thus, energy band structures are primarily determined by $[SbCl_6]^{3-}$ octahedrons. The detailed band alignment is schematically illustrated in Fig. 3b. The calculated work function of 3D phase is 5.82 eV, which is smaller than that of 6.01 eV for 0D phase, indicating that electrons will flow spontaneously from 3D to 0D after the contact of 3D and 0D phases. As a result, the type I heterojunction is created with a built-in electric field from 3D to 0D, and electrons and holes can be simultaneously injected into 0D phase to enhance the green emission of 0D acceptor.

Time-resolved transient absorption (TA) spectroscopy and space-resolved PL mapping were carried out to study charge transfer dynamics and localized emission in 3D/0D heterostructures. 0D phase has a broad photoinduced absorption (PIA) ranging from 500 to 600 nm (Fig. 3c), while 3D phase has a PIA signal ranging from 420 to 500 nm (Supplementary Fig. 11). We can observe a stronger PIA of 0D phase in heterostructures (Fig. 3d) than individual 0D phase (Fig. 3c), indicating the charge transfer occurring from 3D phase to 0D phase. The decay at 460 and 560 nm for 0D phase and 3D/0D heterostructure were fitted by a two-exponential function[44–46]. The fast delay component (τ_1) is assigned to the quenching processes and the long lifetime (τ_2) is ascribed to the recombination of photoinduced electron-hole pairs. Considering the τ_1, we can find that 3D/0D heterostructure (3 ps) has a faster quenching speed than 3D phase (27 ps) at 460 nm but 3D/0D heterostructure (33 ps) has a slower quenching speed than 0D phase (11 ps) at 560 nm (Fig. 3e, f, Supplementary Fig. 12 and Supplementary Table 1). 3D/0D heterostructure also has a shorter PL lifetime than 3D phase (Supplementary Fig. 13). Based on the TA and TRPL kinetics, an efficient charge transfer from 3D phase to 0D phase is demonstrated. Moreover, PL intensity mapping offers the single-particle-level evidence confirming that the enhanced PL intensity of 3D/0D phase compared with 0D phase results from the charge transfer in heterostructures (Supplementary Fig. 14). In particular, PL wavelength mapping and fluorescence microscopy images reveal localized emission within single-particle heterostructures, in contrast to the discrete 3D and 0D emissions observed in the physically mixed phases.

Furthermore, 3D/0D heterostructure has a higher electrical conductivity of ~10^{-2} S m^{-1} compared with that of ~10^{-3} S m^{-1} for 0D phase (Fig. 3g), further confirming the charge transfer behavior[35,47,48]. Figure 3h shows the luminescent mechanism of 3D/0D heterostructures. When individual 3D and 0D phases are exposed by UV or X-ray, the excited electrons are transferred to the corresponding STE states through an energy transfer process, producing corresponding blue and green emissions. In contrast, for 3D/0D type I heterostructures, the charge transfer increases charge density in 0D phase, so a larger energy transfer from $[LuCl_6]^{3-}$ to $[SbCl_6]^{3-}$ is achieved to enhance the STE emission of 0D acceptor. Notably, a direct energy transfer from the $[SbCl_6]^{3-}$ in 3D phase to the $[SbCl_6]^{3-}$ in 0D phase is inhibited by the narrow excitation window of $[SbCl_6]^{3-}$, as observed in the PLE spectra (Supplementary Fig. 10). This provides additional evidence for the charge transfer in 3D/0D heterostructures.

Performances of 3D/0D heterostructure scintillators

We evaluated RL spectra modulation, CT-induced emission, spatial resolution, and irradiation and thermal stabilities of heterostructure scintillators. The RL spectral evolution (Fig. 4a) demonstrates the spectral tunability of 3D/0D heterostructure scintillators. When the proportion of 0D phase exceeds 0.7, sufficient green emission is obtained enabling the white-emitting scintillators. Importantly, we can quantitatively assess the contribution of charge transfer on RL intensity based on the spectrum fitting of heterostructure scintillators (Fig. 4b and Supplementary Figs. 15 and 16). As shown in Fig. 4c, five kinds of heterostructure scintillators have the closed RL intensities. We also find stronger 0D emissions in $3D_{0.1}/0D_{0.9}$ (1.9 times of BGO) and $3D_{0.3}/0D_{0.7}$ (1.6 times of BGO) samples compared to the pure 0D sample (1.3 times of BGO), resulting from the contribution of CT-induced 0D emission (0.7 times of BGO). Moreover, for all heterostructure samples, the RL intensity of CT-induced 0D emission is comparable to that of self-0D emission, despite the diminishing CT contribution with increasing 3D content. Benefiting from the charge transfer, the RL intensity of $3D_{0.3}/0D_{0.7}$ scintillator reaches 2.4 times of BGO, but this RL intensity can drop to only 1.7 times of BGO in the absence of charge transfer. These results demonstrate that the charge transfer can not only enhance the RL intensity of 0D acceptor but also brighten 3D/0D heterostructure scintillators. As a result, the detection limit of 3D/0D heterostructure scintillator (140 nGy_{air} s^{-1}) is much lower than that of 0D scintillator (474 nGy_{air} s^{-1}) (Supplementary Fig. 17). There is a linear relationship between RL intensity and X-ray dose rate, and 3D/0D scintillator has a higher RL intensity than 0D scintillator under different excitation intensities, indicating the charge transfer mechanism in heterostructures. Furthermore, Mn^{2+} is introduced to further improve the red emission of scintillators (Supplementary Fig. 14), and Mn^{2+} dopant does not affect the excitation property of 3D/0D heterostructures (Supplementary Fig. 18).

To address the requirements for high-resolution X-ray imaging, we fabricated a homogeneous composite scintillator screen with a free-standing structure and a large active area (Φ16 cm), as shown in Fig. 4d. We can observe that the scintillator screen has a high spatial resolution of 14 lp mm^{-1} (Fig. 4e), which is confirmed by combining the gray profiles of a line-pair card (Fig. 4f) and the modulation transfer function (MTF) based on the slanted-edge method (Fig. 4g). The definition of contrast is given in Supplementary Note 4.1. When the contrast of an X-ray image is lower than 10% (Fig. 4f), it is considered indistinguishable. Moreover, the RL decay time is close to $Cs_3Cu_2I_5$ due to the same STE emission mechanism[49] (Supplementary Fig. 19).

Finally, we have evaluated irradiation and thermal stabilities of heterostructure scintillators. We can find that the encapsulated scintillator exhibits a robust irradiation stability under a high X-ray dose rate of 20 mGy s^{-1} for the accumulated dose of 1000 Gy (Fig. 4h and Supplementary Fig. 20), which is comparable to $Cs_3Cu_2I_5$[50]. In contrast, the bared scintillator shows an obvious decay in the ambient condition, indicating the Lu-based halides suffer from the similar deliquescence with NaI(Tl). We also find a linearly decreased RL intensity with increasing temperature (Fig. 4i and Supplementary Fig. 21), and 80% RL intensity is remained at 150 °C, which is much higher than that of remained 7% RL for $Cs_3Cu_2I_5$[51]. This superior thermal stability results from its higher Debye temperature[25,52]. More interestingly, we find that Lu-based halide scintillators have increased RL intensity upon irradiation (inset in Fig. 4h) which has rarely been reported. This irradiation-induced RL increase phenomenon may be explained by the incomplete formation of the STE energy for fresh samples, which has been discussed in the $Cs_3Cu_2I_5$ single crystal synthesized using a solution method[53].

Color-integrated X-ray imaging

We developed a color-integrated X-ray imaging technique to enhance the contrast of low-density objects, and both low-density and high-density objects are expected to be discriminated within an image. Different with reported density-discriminating X-ray imaging techniques, including dual-energy X-ray source, vertical matrix detector and stacked chromatic scintillator (Supplementary Note 3)[3–8], our color-integrated X-ray imaging technique depends on a broad-spectrum scintillator and a contrast-enhanced image processing, as shown in Fig. 5a. The contrast-enhanced image processing performs four steps, including color separation, brightness correction, color merging and

https://doi.org/10.1038/s41467-025-62195-x

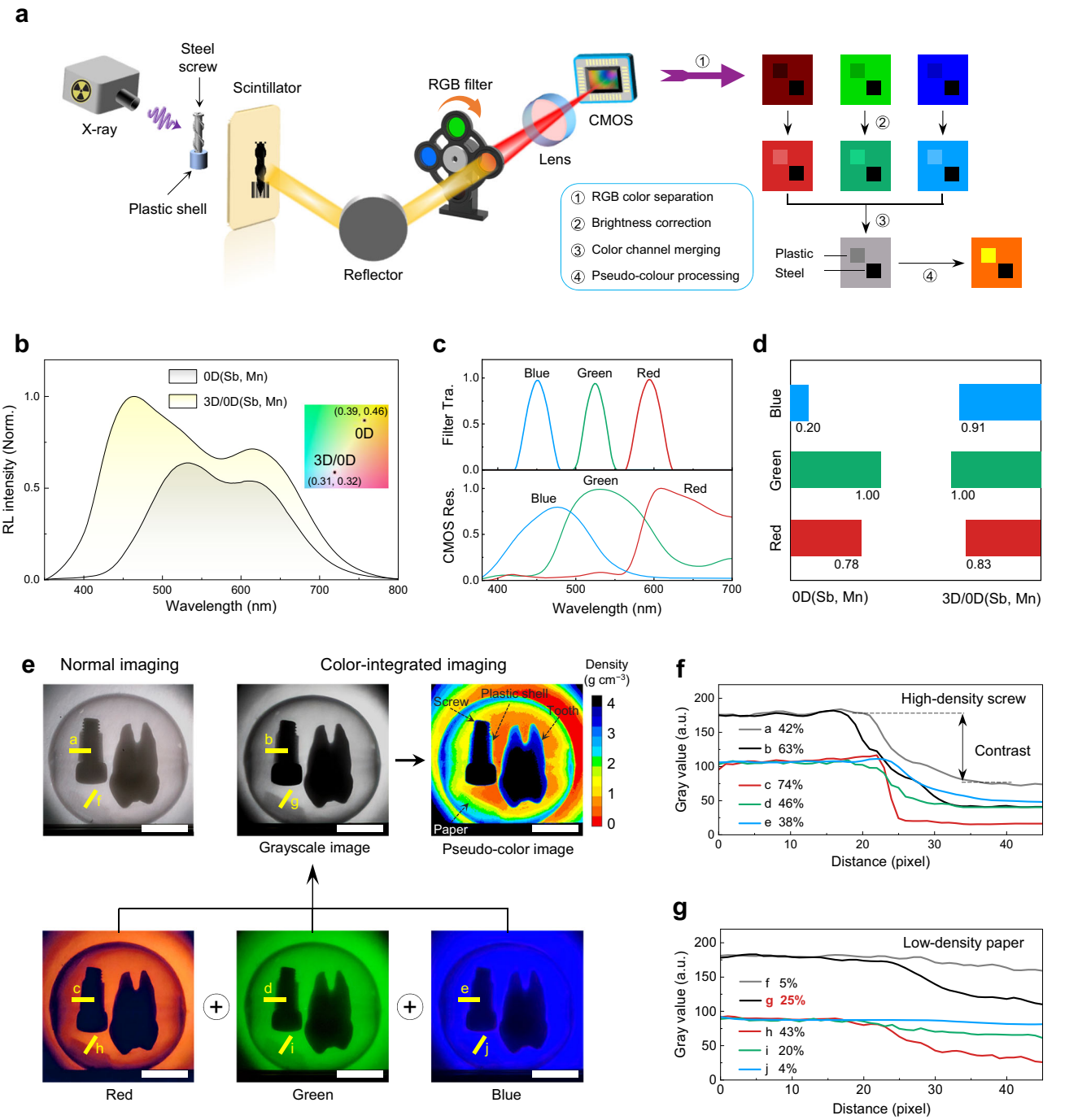

Fig. 5 | Color-integrated X-ray imaging. a A schematic diagram describing the color-integrated X-ray imaging based on a broad-spectrum scintillator and a contrast-enhanced image processing technique. **b** RL spectra of 0D(Sb, Mn) and 3D/0D(Sb, Mn) heterostructure scintillators. Inset is the corresponding chromaticity diagram of CIE 1931. **c** RGB color filter transmission spectra and CMOS responsivity spectra. **d** Output signal intensities of the separated RGB signals. **e** X-ray images obtained from a normal imaging and a color-integrated imaging. Scale bars: 1 cm. The objects are marked in the pseudo-color image. Gray profiles of (**f**) a high-density screw and (**g**) a low-density paper along the lines in (**e**) obtained from two kinds of imaging modes. The numbers beside the letters are calculated contrast values.

pseudo-color processing. Particularly, color separation and merging are essential to ensure that the dark information of low-density objects can be remained, providing an alternative way to extend the dynamic range compared to the reported image intensifier[54,55]. More discussions on the principle can be found in Supplementary Note 4 and Supplementary Figs. 22–25.

First, the spectral properties of heterostructure scintillators were characterized through the color separation process. The broad spectrum of a scintillator is initially separated using color filters, then captured by CMOS pixels, and finally transformed into individual RGB signals (Supplementary Fig. 26). Figure 5b shows that the 3D/0D(Sb, Mn) scintillator has a spectrum-flat and pure-white emission with the CIE color coordinate (0.31, 0.32), compared with the 0D(Sb, Mn) scintillator (0.39, 0.46) and more broad-spectrum scintillators (Supplementary Fig. 27). Combing with filter transmission and CMOS responsivity in Fig. 5c, we can calculate the separated RGB output signals (Fig. 5d and Supplementary Fig. 28). The 3D/0D scintillator exhibits the increased green and red output signals compared with 0D

scintillator, further confirming the contribution of charge transfer on the enhanced 0D emission. Moreover, the 3D/0D(Sb, Mn) scintillator presents the highly balanced RGB output signals (R, G, B = 0.83, 1.00, 0.91) compared with 0D(Sb, Mn) scintillator (R, G, B = 0.78, 1.00, 0.20), CsI(Tl) scintillator (R, G, B = 0.80, 1.00, 0.30) and other broad-spectrum scintillators (Supplementary Table 2). This balanced RGB output is essential for retaining dark information of low-density objects in the contrast-enhanced image processing technique to extend the dynamic range.

Second, the separated RGB images are merged into a grayscale image, which is further converted into a pseudo-color image. As shown in Fig. 5e, a low-density paper cannot be distinguished in the normal X-ray imaging, but it can be well distinguished through a color-integrated imaging technique. In contrast, a high-density screw can be discriminated for both modes. Furthermore, we can observe the density gradient of complex objects (Supplementary Table 3) in the pseudo-color image, and both low-density and high-density objects can be distinguished within an image. Quantitatively, a low-density paper with a contrast of 25% obtained from the color-integrated imaging is significantly higher than that of 5% from the normal imaging (Fig. 5f, g), demonstrating the role of the color-integrated imaging in improving the contrast of low-density object. The contrast of a high-density screw is also slightly improved through the color-integrated imaging. In contrast, a broad-spectrum CsI(Tl) scintillator cannot achieve an obvious contrast enhancement for a low-density object with a small contrast of 7% (Supplementary Fig. 29), and this inferior performance results from the unbalanced RGB output caused by the CsI(Tl) scintillator with the absence of spectrum-flat emission. More discussions are given in Supplementary Note 4.3. Therefore, a spectrum-flat white scintillator enabling a balanced RGB output is essential to distinguish the low-density objects in color-integrated X-ray imaging.

In summary, we synthesize 3D/0D Lu-based halide heterostructures through a Na-alloying strategy, which is a facile method to synthesize composition-modulated lead-free metal halide heterostructures. The 3D/0D heterostructures are constructed by the structural transformation from 0D phase to 3D phase, and the spectral intensity and linewidth of scintillators are tailored simultaneously by the charge transfer in 3D/0D heterostructures. The charge transfer from 3D phase to 0D phase is corroborated based on the theoretical energy band alignment, as well as the experimental spectral transient dynamics, microscopic PL, and electrical conductivity. Benefiting from a high charge transfer efficiency in type I heterostructure, the 3D/0D scintillator has a much higher RL intensity (2.4 times of BGO) than that of 0D scintillator (1.3 times of BGO). Meanwhile, the 3D/0D heterostructure scintillator has realized a spectrum-flat and pure-white emission, because charge transfer can improve green and red emissions of 0D acceptor. Importantly, the 3D/0D scintillator with balanced RGB output signals enables to extend the dynamic range in color-integrated X-ray imaging. These findings shed light on the charge transfer mechanism in lead-free metal halide heterostructures and provide a promising white-emission scintillator for the X-ray imaging application.

Methods

Chemicals

CsCl (99.9%), NaCl (99.9%), $LuCl_3{\cdot}6H_2O$ (99.9%), $SbCl_3$ (99.9%), and $MnCl_2$ (99.9%) were purchased from Innochem. Hydrochloric acid (HCl, 37 wt% in water) was purchased from Macklin. All of the chemicals were used as received without further purification.

Synthesis of microcrystal powders

Microcrystal powders were synthesized following the modified HCl-assistant powder method[41]. Metal salt powders were mixed with HCl and stirred for 10 min. The product was centrifuged at 447 × *g* and washed by ethanol for twice. The collected product was transferred to a 60 °C oven to dry and then annealed at 400 °C for 2 h. For the synthesis of $Cs_2NaLuCl_6$, 4 mmol of CsCl, 2 mmol of NaCl and 2 mmol of $LuCl_3{\cdot}6H_2O$ were used. For the synthesis of Cs_3LuCl_6, 6 mmol of CsCl and 2 mmol of $LuCl_3{\cdot}6H_2O$ were used. For the synthesis of 3D/0D heterostructure, a variable ratio of NaCl water solution was added into Cs_3LuCl_6 reaction system, and emission color changed immediately. For Sb-doped and Sb/Mn co-doped samples, varying ratios of $SbCl_3$ and $MnCl_2$ solutions were added.

Scintillator fabrication

Inorganic powders and polyethylene were ground in an automatic grinder machine to achieve a uniform mixture, and the mixture was loaded in a mold under a pressure of 10 MPa at 150 °C to form an inorganic particle/polymer composite scintillator with the thickness of 0.2 mm. The weight fraction of inorganic powder was 50 wt%. For thermal measurement, polydimethylsiloxane (PDMS) matrix was used to host inorganic powders. For air irradiation measurement, transparent epoxy resin was used to encapsulate composite scintillator screen, avoiding air exposure.

Characterization

Scanning electron microscope (SEM) was conducted on a ZEISS Gemini 300. Transmission electron microscope (TEM) was performed on a JEM-2100F with a Ultim Max 80 detector (element mapping). High-resolution TEM (HRTEM), high-angle annular dark-field (HAADF), and elemental mapping were characterized. X-ray diffraction (XRD) was carried out with a Bruker D8 Advance using Cu Kα radiation. The optical absorption spectra were collected with a Hitachi UV-Visible spectrophotometer UH5700. The PL and TRPL spectra were acquired with a FLS980 spectrometer. TA measurements were performed on a Helios (Ultrafast systems) spectrometers using a regeneratively amplified femtosecond Ti:sapphire laser system (Spitfire Pro-F1KXP, Spectra-Physics; frequency, 1 kHz; max pulse energy, ~8 mJ; pulse width, 120 fs) at room temperature. Inorganic particles were transferred on a pair of Au electrodes with a gap width of 6 μm, and current-voltage curves were collected in the dark by a photodetector measurement instrument. The stable electrical signals could be obtained after multiple electrical cycles to guarantee the closed contact between particles and electrodes. Two kinds of particles with the closed size were used to exclude the possible volume effect, and a single particle was used to minimize the impact of grain boundary. Fluorescence microscopy images were collected when all samples were excited under a 365 nm LED, and narrow-band optical filters (450, 530, and 620 nm) were added to identify 3D (blue) and 0D (green) emissions. PL intensity and wavelength mapping were performed on a Zolix microscopic PL system, and powders on Si substrates were excited under a 365 nm laser. The pixel size of PL mapping was 5 μm which is close to the size of single inorganic microcrystal particle.

RL measurement

X-ray dose rate was measured with an XR detector (MagicMaX Universal). The X-ray excited emission spectra were recorded by a spectrophotometer (B&W TEK Exemplar Plus LS). For RL spectra measurement, the X-ray source was Amptek Mini-X2 with the voltage of 50 kV and the current of 100 μA. The X-ray dose rate was 0.5 mGy s^{-1} and the integrated time was 5 s. The relative RL intensities of scintillators were determined by comparison with a BGO wafer with the same size. The RL decay of scintillators was acquired by an oscilloscope with connecting to a photomultiplier tube and excited by a pulsed X-ray generator (Golden, XRS-4). For X-ray irradiation stability measurement, an industrial X-ray source (Beijing Kaiwei Xinda Technology Co., Ltd) was continuously operated at the 60 kV and 1 mA with the assistance of a heat dissipation system. Scintillators were irradiated with the X-ray dose rate was 20 mGy s^{-1}. A thin composite scintillator has an X-ray absorption efficiency of 45%, which is lower than that of 100% for

CsI(Tl) single crystal. Each RL spectra was collected for the time interval of 10 min. For temperature-dependence measurement, a flexible PI heater was pasted on scintillators to ensure the uniform heating.

X-ray imaging measurement

X-ray imaging was acquired by a CMOS camera (Tucsen FL-20) equipped with a prime lens (AZURE-5022ML12M) or a microscopic lens (Coosway, CSW-0650). The spatial resolution was evaluated by a standard line-pair card (0.03 mm Pb, CN89727), which was further verified based on the slanted-edge method. The contrast-enhanced image processing was conducted following next four steps. First, red (600 nm), green (525 nm) and blue (450 nm) color filters with the narrowband of 40 nm were individually introduced to obtain the separated RGB images. Second, the brightness correction of three-color images was required due to color-dependent responsivity of CMOS sensor. Third, the RGB channels were combined into a grayscale image using Photoshop's channel merging function, and the grayscale value represents the object's density. Finally, a pseudo-color image was created through a color conversion process using the 16-color lookup table (LUT) function in ImageJ software. This process enables the intuitive display of density gradient in the imaging objects based on the color representation in the pseudo-color image.

Density functional theory

The decomposition enthalpy and electronic structures were calculated using the Vienna Ab initio Simulation Package (VASP). The Perdew-Burke-Ernzerhof (PBE) exchange-correlation functional combining with generalized gradient approximation (GGA) method was utilized to obtain the lattice constants. The energy cutoff was set to 500 eV for the plane-wave function's expansion. The Γ-centered $5 \times 5 \times 5$ Monkhorst-Pack grid k-points were used to sample the Brillouin zone integration for structural optimization while the open-source package VASPKIT was further applied to generated corresponding k-points with high symmetry. The decomposition compounds NaCl, Cs_3LuCl_6, and $LuCl_3$ are sampled with $7 \times 7 \times 7$, $1 \times 1 \times 1$, and $5 \times 5 \times 6$ k-point grids. In all geometric optimization, the residual force was converged until the total energy changes were less than 1.0×10^{-5} eV and the maximum force component acting on each atom was less than 0.01 eV $Å^{-1}$.

Data availability

The source data generated in this study have been deposited in the figshare database under accession code https://doi.org/10.6084/m9.figshare.29178554. Additionally, all data are available from the corresponding authors upon request. Correspondence and requests for materials should be addressed to Z.Y. or J.S.

References

1. Hou, B. et al. Materials innovation and electrical engineering in X-ray detection. *Nat. Rev. Electr. Eng.* **1**, 639–655 (2024).
2. Ou, X. et al. Recent development in X-ray imaging technology: future and challenges. *Research* **2021**, 892152 (2021).
3. Pang, J. et al. Vertical matrix perovskite X-ray detector for effective multi-energy discrimination. *Light Sci. Appl.* **11**, 105 (2022).
4. Ran, P. et al. Multispectral large-panel X-ray imaging enabled by stacked metal halide scintillators. *Adv. Mater.* **34**, 2205458 (2022).
5. Hu, X. et al. Density-discriminating chromatic X-ray imaging based on metal halide nanocrystal scintillators. *Sci. Adv.* **9**, eadh5081 (2023).
6. Shao, W. et al. Transparent organic and metal halide tandem scintillators for high-resolution dual-energy X-ray imaging. *ACS Energy Lett.* **8**, 2505–2512 (2023).
7. He, T. et al. Multi-energy X-ray imaging enabled by ΔE-E telescope scintillator. *Matter* **7**, 2521–2535 (2024).
8. Hui, J. et al. Stacked scintillators based multispectral X-ray imaging featuring quantum-cutting perovskite scintillators with 570 nm absorption-emission shift. *Adv. Mater.* **37**, 2416360 (2025).
9. Xu, L., Lin, X., He, Q., Worku, M. & Ma, B. Highly efficient eco-friendly X-ray scintillators based on an organic manganese halide. *Nat. Commun.* **11**, 4329 (2020).
10. Zhu, W. et al. Low-dose real-time X-ray imaging with nontoxic double perovskite scintillators. *Light Sci. Appl.* **9**, 112 (2020).
11. Wu, H. et al. One-dimensional scintillator film with benign grain boundaries for high-resolution and fast X-ray imaging. *Sci. Adv.* **9**, eadh1789 (2023).
12. Han, K. et al. Hybrid Eu(II)-bromide scintillators with efficient 5d-4f bandgap transition for X-ray imaging. *Light Sci. Appl.* **13**, 222 (2024).
13. Zhang, F. et al. Thermally activated delayed fluorescence zirconium-based perovskites for large-area and ultraflexible X-ray scintillator screens. *Adv. Mater.* **34**, 2204801 (2022).
14. Yang, B. et al. Lead-free halide Rb_2CuBr_3 as sensitive X-ray scintillator. *Adv. Mater.* **31**, 1904711 (2019).
15. Han, P. et al. All-inorganic lead-free 0D perovskites by a doping strategy to achieve a PLQY boost from <2% to 90%. *Angew. Chem.* **132**, 12809–12813 (2020).
16. Zhao, S. et al. White emission metal halides for flexible and transparent X-ray scintillators. *Appl. Phys. Rev.* **11**, 011408 (2024).
17. Ju, D. et al. Excitation-selective and double-emissive lead-free binary hybrid metal halides for white light-emitting diode and X-ray scintillation. *Small* **20**, 2305083 (2024).
18. Huang, H. et al. Accommodative organoammonium cations in A-sites of Sb-In halide perovskite derivatives for tailoring broadband photoluminescence with X-Ray scintillation and white-light emission. *Adv. Funct. Mater.* **34**, 2309112 (2024).
19. Lin, R. et al. Self-assembled eco-friendly metal halide heterostructures for bright and color-tunable white radioluminescence. *Cell Rep. Phys. Sci.* **2**, 100437 (2021).
20. Li, H. et al. A Solar-blind perovskite scintillator realizing portable X-ray imaging. *ACS Energy Lett.* **7**, 2876–2883 (2022).
21. Yang, Z. et al. Fiber optic plate coupled Pb-free perovskite X-ray camera featuring low-dose-rate imaging toward dental diagnosis. *J. Phys. Chem. Lett.* **14**, 326–333 (2023).
22. Xiao, Z., Song, Z. & Yan, Y. From lead halide perovskites to lead-free metal halide perovskites and perovskite derivatives. *Adv. Mater.* **31**, 1803792 (2019).
23. Zhang, M. et al. Molecular engineering towards efficient white-light-emitting perovskite. *Nat. Commun.* **12**, 4890 (2021).
24. Li, S., Luo, J., Liu, J. & Tang, J. Self-trapped excitons in all-inorganic halide perovskites: fundamentals, status, and potential applications. *J. Phys. Chem. Lett.* **10**, 1999–2007 (2019).
25. Kim, H. W. et al. High-throughput screening on halide perovskite derivatives and rational design of Cs_3LuCl_6. *ACS Energy Lett.* **8**, 3621–3630 (2023).
26. Dorenbos, P., van Loef, E. V. D., van Eijk, C. W. E., Krämer, K. W. & Güdel, H. U. Anomalous 10-ns emission in Ce^{3+}-doped Cs_3LuCl_6. *Phys. Rev. B* **68**, 125108 (2003).
27. Chen, C. et al. Blue-red dual color emitting phosphor $Cs_2NaLuCl_6$: Sb^{3+}, Ho^{3+} for plant growth LEDs. *Ceram. Int.* **49**, 25232–25239 (2023).
28. Li, X. et al. Lead-free Ce-doped perovskite scintillators with high figure of merit. *J. Energy Chem.* **99**, 74–82 (2024).
29. Birowosuto, M. D., Dorenbos, P., van Eijk, C. W. E., Krämer, K. W. & Güdel, H. U. Scintillation properties and anomalous Ce^{3+} emission of $Cs_2NaREBr_6$:Ce^{3+} (RE = La, Y, Lu). *J. Phys. Condens. Matter* **18**, 6133 (2006).
30. Cao, F. et al. Shining emitter in a stable host: design of halide perovskite scintillators for X-ray imaging from commercial concept. *ACS Nano* **14**, 5183–5193 (2020).

31. Naresh, V., Singh, S., Soh, H., Lee, J. & Lee, N. Dual-phase $CsPbBr_3$-$CsPb_2Br_5$ perovskite scintillator for sensitive X-ray detection and imaging. *Mater. Today Nano* **23**, 100364 (2023).
32. Zhang, J., Zhu, X., Wang, M. & Hu, B. Establishing charge-transfer excitons in 2D perovskite heterostructures. *Nat. Commun.* **11**, 2618 (2020).
33. Shi, E. et al. Two-dimensional halide perovskite lateral epitaxial heterostructures. *Nature* **580**, 614–620 (2020).
34. Pan, D. et al. Deterministic fabrication of arbitrary vertical heterostructures of two-dimensional Ruddlesden–Popper halide perovskites. *Nat. Nanotechnol.* **16**, 159–165 (2021).
35. Zhu, Z. et al. Room-temperature epitaxial welding of 3D and 2D perovskites. *Nat. Mater.* **21**, 1042–1049 (2022).
36. Yang, Z., Yao, J., Xu, L., Fan, W. & Song, J. Designer bright and fast $CsPbBr_3$ perovskite nanocrystal scintillators for high-speed X-ray imaging. *Nat. Commun.* **15**, 8870 (2024).
37. Gu, L. et al. Achieving high loading capacity of perovskite nanocrystals in pore-reamed metal–organic frameworks for bright scintillators. *ACS Nano* **19**, 15803–15812 (2025).
38. Zhang, G. et al. Boosting energy transfer from self-trapped exciton to Er^{3+} through Sb^{3+} doping in $Cs_2Na(Lu/Er)Cl_6$ double perovskites. *Adv. Opt. Mater.* **11**, 2202369 (2023).
39. Zhou, B. et al. Emission mechanism of self-trapped excitons in Sb^{3+}-doped all-inorganic metal-halide perovskites. *J. Phys. Chem. Lett.* **13**, 9140–9147 (2022).
40. Zeng, R. et al. Highly efficient blue emission from self-trapped excitons in stable Sb^{3+}-doped $Cs_2NaInCl_6$ double perovskites. *J. Phys. Chem. Lett.* **11**, 2053–2061 (2020).
41. Yang, H. et al. A universal hydrochloric acid-assistant powder-to-powder strategy for quick and mass preparation of lead-free perovskite microcrystals. *Light Sci. Appl.* **12**, 75 (2023).
42. Guo, X. X. et al. Tailoring the emission properties of $Cs_2NaLuCl_6$ for anti-counterfeiting, X-Ray scintillation, and night vision applications. *Adv. Opt. Mater.* **13**, 2402845 (2025).
43. Noculak, A. et al. Bright blue and green luminescence of Sb(III) in double perovskite Cs_2MInCl_6 (M = Na, K) matrices. *Chem. Mater.* **32**, 5118–5124 (2020).
44. Zhou, B. et al. Modulating adsorption–redox sites and charge separation of $Cs_3Bi_2Br_{9-x}$@AgBr core–shell heterostructure for selective toluene photooxidation. *ACS Energy Lett.* **9**, 1743–1752 (2024).
45. Lin, C., Tang, Y., Xu, W., Kumar, P. & Dou, L. Charge transfer in 2D halide perovskites and 2D/3D heterostructures. *ACS Energy Lett.* **9**, 3877–3886 (2024).
46. Chen, X., Kamat, P. V., Janáky, C. & Samu, G. F. Charge transfer kinetics in halide perovskites: on the constraints of time-resolved spectroscopy measurements. *ACS Energy Lett.* **9**, 3187–3203 (2024).
47. Singh, N., Malik, A., Sethi, P. & Mondal, P. C. Programmed heterostructures for enhanced electrical conductivity. *Small* **20**, 2403108 (2024).
48. Luo, Z.-Z. et al. Multifunctional 0D-2D Ni_2P nanocrystals-black phosphorus heterostructure. *Adv. Energy Mater.* **7**, 1601285 (2017).
49. Stand, L. et al. Crystal growth and scintillation properties of pure and Tl-doped $Cs_3Cu_2I_5$. *Nucl. Instrum. Meth. A* **991**, 164963 (2021).
50. Gao, L., Li, Q., Sun, J.-L. & Yan, Q. Gamma-ray irradiation stability of zero-dimensional $Cs_3Cu_2I_5$ metal halide scintillator single crystals. *J. Phys. Chem. Lett.* **14**, 1165–1173 (2023).
51. Li, X. et al. Mn^{2+} induced significant improvement and robust stability of radioluminescence in $Cs_3Cu_2I_5$ for high-performance nuclear battery. *Nat. Commun.* **12**, 3879 (2021).
52. Ali, M. L., Khan, M., Al Asad, M. A. & Rahaman, M. Z. Highly efficient and stable lead-free cesium copper halide perovskites for optoelectronic applications: a DFT based study. *Heliyon* **9**, e18816 (2023).
53. Ma, Y. et al. Exploring the mystery of "negative thermal quenching" in $Cs_3Cu_2I_5$ single-crystal. *Adv. Opt. Mater.* **13**, 2403194 (2025).
54. Nittoh, K., Oyaizu, E., Sakurai, T., Yoshida, T. & Mochiki, K.-I. Extension of dynamic range in X-ray radiography using multi-color scintillation detector. *Nucl. Instrum. Meth. A* **501**, 615–622 (2003).
55. Nittoh, K., Konagai, C. & Noji, T. Development of multi-color scintillator based X-ray image intensifier. *Nucl. Instrum. Meth. A* **535**, 686–691 (2004).

Acknowledgements

This research was financially supported by the National Natural Science Foundation of China (NSFC Grant No. 52272166) and the Natural Science Foundation of Henan Province (232300421214 and 242300421217).

Author contributions

J.S. and Z.Y. conceived and supervised the project. Z.Y., J.C., and Y.S. conducted and analyzed the experiments. J.Y. and S.Y. assisted in the Figure preparation and manuscript revision. Z.Y. and J.S. wrote the manuscript. All authors contributed to the general discussion and reviewed the paper.

Competing interests

The authors declare no competing interests.

Additional information

Supplementary information The online version contains supplementary material available at https://doi.org/10.1038/s41467-025-62195-x.

Correspondence and requests for materials should be addressed to Zhi Yang or Jizhong Song.

Peer review information *Nature Communications* thanks Guangda Niu and the other anonymous reviewer(s) for their contribution to the peer review of this work. A peer review file is available.